

Maximizing the electromomentum coupling in piezoelectric laminates

Majd Kosta¹, Alan Muhafara², Rene Pernas-Salómon^{*2}, Gal Shmuel², and Oded Amir¹

¹Faculty of Civil Engineering, Technion–Israel Institute of Technology, Haifa 32000, Israel

²Faculty of Mechanical Engineering, Technion–Israel Institute of Technology, Haifa 32000, Israel

Abstract

Asymmetric piezoelectric composites exhibit coupling between their macroscopic linear momentum and electric field, a coupling that does not appear at the microscopic scale. This electromomentum coupling constitutes an additional knob to tailor the dynamic response of the medium, analogously to the Willis coupling in elastic composites. Here, we employ topology- and free material optimization approaches to maximize the electromomentum coupling of periodic piezoelectric laminates in the low frequency, long-wavelength limit. We find that the coupling can be enhanced by orders of magnitude, depending on the degrees of freedom in the optimization process. The optimal compositions that we find provide guidelines for the design of metamaterials with maximum electromomentum coupling, paving the way for their integration in wave control applications.

1 Introduction

Metamaterials are artificial composites whose effective behavior is fundamentally different from the behavior of their constituents [1–10]. Of particular relevance to this work are Willis metamaterials [11–31], whose linear momentum and strain is coupled, and so are their stress and velocity: these couplings do not appear in homogeneous media. They are captured by the so-called Willis tensor that enters the effective constitutive relations of the composite, reflecting a designable degree of freedom to tailor its dynamic response. The Willis tensor is nonlocal in space and time; its

^{*}Present address: Universidad Carlos III de Madrid, Avenida de la Universidad 30, 28911, Leganés, Spain.

(spatially) local version was introduced by Milton et al. [32], and a model that demonstrates such behavior was developed later by Milton [33].

Recently, Pernas-Salomón and Shmuel [34] have generalized the Willis couplings to piezoelectric composites, discovering that their linear momentum and electric displacement field can be macroscopically coupled with the electric field and velocity, respectively. This effect is captured by a second-order tensor—the *electromomentum* tensor—that enters the effective constitutive relations of the piezoelectric composites. Analogously to the Willis tensor, the electromomentum tensor not only constitutes an additional knob to tailor the dynamic response of the medium, but is also necessary for obtaining a physical constitutive description [35–37].

The objective of this work is to maximize the electromomentum effect in periodic piezoelectric laminates driven by axial load sources. The poling direction of the piezoelectric constituents is also in the lamination direction, such that the problem is one-dimensional, and the electromomentum tensor becomes a scalar material property. We further restrict attention to the low frequency, long-wavelength limit, where the electromomentum coefficient depends linearly on the frequency, and is local in space. The motivation for identifying laminates with large electromomentum coefficient is twofold. First, it makes more pronounced the phenomena that the electromomentum effect generate, such as the change in the phase velocity and directional phase angle of elastic waves [36]. Second, the optimal compositions are expected to elucidate the dependency of the electromomentum coupling on the mechanical and geometrical properties of the constituents. Very recently, a preliminary work towards this end was done by Zhang et al. [38]. There, the authors studied 8-layer unit cells made of five real materials, and examined how the electromomentum coefficient changes as function of the different material combinations and layer thickness. Here, we take a different route, using optimization methods. Specifically, our approach is based on topology- and free material optimization (FMO) methods: topology optimization aims to determine the optimal material distribution for a designated objective function in a given design space [39]; FMO [40–42] is an extension of topology optimization, in which each material property can vary independently of the other properties. Since the design space for FMO is free from the constraint of real materials, it provides a kind of a theoretical upper bound for the objective function.

The objective function, i.e., the electromomentum coefficient, is formulated as the end result of a homogenization process. In this process, the heterogeneous constitutive properties of the composite are replaced by fictitious homogeneous constitutive properties, relating the macroscopic kinematic variables to the macroscopic kinetic variables. Further details regarding the homogenization scheme are given in Section 2. Accordingly, the optimization methods that we apply are in fact inverse homogenization methods [43] for the constitutive property.

Our analysis begins in Section 3 with discrete material optimization, or DMO [44, 45], where the design space is a predefined set of real materials. For simplicity, here and in the subsequent

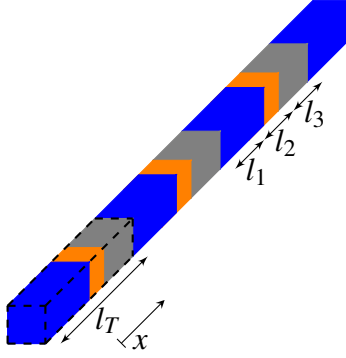


Figure 1: Part of an infinite medium made of a periodic cell with three layers. The length of the first, second and third layer is denoted by l_1 , l_2 and l_3 , respectively. The elementary unit cell is boxed in dashed lines, where $l_T = \sum_{m=1}^3 l_m$.

optimization problems, we restrict attention to periodic cells that are made of three layers. Since this optimization is based on a small number of discrete variables, we use a genetic algorithm to solve the optimization problem. We find that the electromomentum coefficient of the optimal laminate is two orders of magnitude larger than the laminate that was first considered by Pernas-Salomón and Shmuel [34], which was chosen arbitrarily. Henceforth, we refer to the latter laminate as the reference laminate. We observe that the optimization yields a choice of materials that tends to maximize the contrast between their electromechanical properties, in a unit cell that comprises one thin layer in-between two thick layers.

In Section 4 we consider a design space with continuous variables, whose values are bounded in-between the extreme values of the materials considered earlier. We solve different optimization problems using gradient-based algorithms that are implemented together with a sensitivity analysis of the objective function. We first consider optimization problems whose design variables are pairs that consist the mass density and one of the electromechanical properties, i.e., the dielectric-, piezoelectric- and stiffness coefficients, while all the rest of the properties are set to the properties of the reference laminate. We find that each one of the optimal pairs enlarge the electromomentum coefficient by another order of magnitude, in comparison with the optimal laminate that is obtained from the DMO. We then proceed and increase the number of design variables, and find that when all material properties are designable, the electromomentum coefficient is enlarged by another order of magnitude. We conclude this paper in Section 5, with a summary of our main results.

2 The homogenization process

The homogenization process that we use to extract the electromomentum coefficient is founded on two principles. (i) The macroscopic fields are defined by the product of the Bloch envelope of the microscopic fields and the volume average of their periodic part. Defined in this way, the

effective fields satisfy identically macroscopic governing equations that are of the same form as the microscopic equations, see Refs. [34, 46, 47]. (ii) We account for several driving sources in the formulation [34, 46, 48–50]; collectively, these sources allow us to obtain a *unique* set of effective properties [17, 51–53], which satisfies necessary physical laws [16, 37, 52, 54, 55].

Our averaging process uses the plane wave expansion method [18, 23, 56–58], and the resultant scheme is essentially a one-dimensional reduction of the scheme that was developed by Muhafra et al. [37]. In order to make this manuscript self-contained and introduce the quantities that are used in the optimization process, the complete one-dimensional scheme is provided next.

Consider a periodic repetition of three piezoelectric layers, the poling direction of which is in the lamination direction, say x . The laminate is driven by a body force density f , axial inelastic strain η , and free charge density q , of the form

$$s(x, t) = s^0 e^{i(\kappa x - \omega t)}, \quad s = \eta, f, q, \quad (1)$$

where $\{s^0\}$ are constant. These sources generate a longitudinal motion, $u(x, t)$, governed by the equations

$$\sigma_{,x} + f = p_{,t}, \quad D_{,x} = q; \quad (2)$$

here, σ is the Cauchy stress, p is the linear momentum, and D is the electric displacement. The remaining Faraday equation for electric field E is satisfied by setting $E = -\phi_{,x}$, where ϕ is termed the electric potential. The microscopic kinetic and kinematic fields in the laminate are related via the constitutive relations

$$\begin{pmatrix} \sigma \\ D \\ p \end{pmatrix} = \begin{pmatrix} C & B & 0 \\ B & -A & 0 \\ 0 & 0 & \rho \end{pmatrix} \begin{pmatrix} u_{,x} - \eta \\ \phi_{,x} \\ u_{,t} \end{pmatrix}, \quad (3)$$

where C , B , A and ρ are the stiffness, piezoelectric coefficient, dielectric coefficient and the mass density, respectively. These properties are periodic, such that

$$\xi(x + nl_T) = \xi(x), \quad \xi = C, B, A, \rho, \quad (4)$$

where $n \in \mathbb{Z}$; $l_T = \sum_{m=1}^3 l_m$ and l_m is the length of layer m , as shown in Figure 1. This periodicity implies that the kinetic and the kinematic fields are of the Bloch form

$$\alpha(x, t) = \hat{\alpha}(x) e^{i(\kappa x - \omega t)}, \quad \hat{\alpha}(x + nl_T) = \hat{\alpha}(x), \quad \alpha = \sigma, D, p, u, \phi. \quad (5)$$

The objective is to determine the effective constitutive relations, relating the macroscopic fields,

which have the form

$$\langle \alpha \rangle(x, t) = \bar{\alpha} e^{i(\kappa x - \omega t)}, \quad \bar{\alpha} = l_T^{-1} \int_{l_T} \hat{\alpha}(x) dx. \quad (6)$$

To this end, we first consider the Bloch form of Eq. (3), namely,

$$\begin{pmatrix} \hat{\sigma}(x) \\ \hat{D}(x) \\ \hat{p}(x) \end{pmatrix} e^{i(\kappa x - \omega t)} = \begin{pmatrix} C(x) & B^\top(x) & 0 \\ B(x) & -A(x) & 0 \\ 0 & 0 & \rho(x) \end{pmatrix} \begin{pmatrix} \hat{u}(x)_{,x} + i\kappa \hat{u}(x) - \hat{\eta}(x) \\ \hat{\phi}(x)_{,x} + i\kappa \hat{\phi}(x) \\ -i\omega \hat{u}(x) \end{pmatrix} e^{i(\kappa x - \omega t)}. \quad (7)$$

To relate the mean parts of the kinetic and kinematic fields, we expand the periodic functions in Eq. (7) in Fourier series, such that

$$\hat{\psi}(x) = \sum_G \check{\psi}_G e^{iGx}, \quad \check{\psi}_G = l_T^{-1} \int_{l_T} \hat{\psi}(x) e^{-iGx} dx, \quad \hat{\psi} = \hat{\alpha}, \xi, \quad (8)$$

where $\{\check{\psi}_G\}$ are the Fourier coefficients of $\hat{\psi}(x)$; $G = \frac{2\pi}{l_T} m$ and $m \in \mathbb{Z}$. Substituting Eq. (8) into Eq. (7) yields

$$\left[\sum_G \begin{pmatrix} \check{\sigma}_G \\ \check{D}_G \\ \check{p}_G \end{pmatrix} e^{iGx} - \sum_{G, G'} \begin{pmatrix} \check{C}_G & \check{B}_G^\top & 0 \\ \check{B}_G & -\check{A}_G & 0 \\ 0 & 0 & \check{\rho}_G \end{pmatrix} \begin{pmatrix} i(\kappa + G') \check{u}_{G'} - \check{\eta}_{G'} \\ i(\kappa + G') \check{\phi}_{G'} \\ -i\omega \check{u}_{G'} \end{pmatrix} e^{i(G+G')x} \right] e^{i(\kappa x - \omega t)} = \begin{pmatrix} 0 \\ 0 \\ 0 \end{pmatrix}, \quad (9)$$

where G' is defined in the same manner as G and Eq. (9) contains every combination of G' and G . Since Eq. (9) holds for any value of x and t , the sum in the square brackets must be zero. We multiply those sums by $e^{-iG''x}$, and integrate the result over the unit cell. Due to the orthogonality property of the Fourier series, the only non-vanishing terms are those satisfying the condition $G'' = G + G'$. Hence, substituting $G'' = G$ into the resultant equation yields

$$\begin{pmatrix} \check{\sigma}_G \\ \check{D}_G \\ \check{p}_G \end{pmatrix} = \sum_{G'} \begin{pmatrix} \check{C}_{GG'} & \check{B}_{GG'}^\top & 0 \\ \check{B}_{GG'} & -\check{A}_{GG'} & 0 \\ 0 & 0 & \check{\rho}_{GG'} \end{pmatrix} \begin{pmatrix} i(\kappa + G') \check{u}_{G'} - \check{\eta}_{G'} \\ i(\kappa + G') \check{\phi}_{G'} \\ -i\omega \check{u}_{G'} \end{pmatrix}, \quad (10)$$

where $(\circ)_{GG'}$ denotes the Fourier coefficient of (\circ) along the basis function $e^{i(G-G')x}$. In the same manner, Eq. (2) reads

$$\begin{aligned} (\hat{\sigma}_{,x} + i\kappa \hat{\sigma} + \hat{f}) e^{i(\kappa x - \omega t)} &= -i\omega \hat{p} e^{i(\kappa x - \omega t)}, \\ (\hat{D}_{,x} + i\kappa \hat{D}) e^{i(\kappa x - \omega t)} &= \hat{q} e^{i(\kappa x - \omega t)}. \end{aligned} \quad (11)$$

Once again, we expand the periodic parts to

$$\begin{aligned} \sum_G [i(\boldsymbol{\kappa} + G) \check{\sigma}_G + \check{f}_G] e^{iGx} e^{i(\boldsymbol{\kappa}x - \omega t)} &= -i\omega \sum_G \check{p}_G e^{iGx} e^{i(\boldsymbol{\kappa}x - \omega t)}, \\ \sum_G [i(\boldsymbol{\kappa} + G) \check{D}_G] e^{iGx} e^{i(\boldsymbol{\kappa}x - \omega t)} &= \sum_G \check{q}_G e^{iGx} e^{i(\boldsymbol{\kappa}x - \omega t)}. \end{aligned} \quad (12)$$

A truncation to a finite number of plane waves N is carried out for implementational purposes, say by $-s \leq m \leq s$ ¹, such that $N = 2s + 1$. We multiply those sums by $e^{-iG''x}$, and integrate the result over the unit cell. Due to the orthogonality property of the Fourier series, the only non-vanishing terms are those satisfying the condition $G'' = G$. We can write for each G

$$D_G^T h_G = -f_G, \quad (13)$$

where

$$D_G = \begin{pmatrix} i(\boldsymbol{\kappa} + G) & 0 \\ 0 & i(\boldsymbol{\kappa} + G) \\ i\omega & 0 \end{pmatrix}, h_G = \begin{pmatrix} \check{\sigma}_G \\ \check{D}_G \\ \check{p}_G \end{pmatrix}, f_G = \begin{pmatrix} \check{f}_G \\ -\check{q}_G \end{pmatrix}. \quad (14)$$

We assemble all the equations of each G into a single matrix system, namely,

$$D_A^T h_A = -f_A, \quad (15)$$

where f_A is a column vector of $2N$ components that assembles all the Fourier coefficients of \check{f}_G and \check{q}_G ; h_A is a column vector of $3N$ components, which assembles all the Fourier coefficients of $\check{\sigma}_G, \check{D}_G$ and \check{p}_G ; and D_A is a $3N \times 2N$ matrix that is composed from 3 diagonal and 3 zero matrices. For further details the reader is referred to Appendix B. In the same manner, h_A is expressed by assembling the matrix equations of the constitutive relation in Eq. (10), namely,

$$h_A = L_A (J_A w_A - m_A), \quad (16)$$

where L_A is a $3N \times 3N$ matrix that contains the Fourier components of the material properties. Similarly to D_A , J_A is a $3N \times 2N$ matrix that is composed from 3 diagonal and 3 zero matrices; w_A is a column vector of $2N$ coefficients that assembles the Fourier components of the electric potential the displacement; and m_A is a column vector of $3N$ components that contains the Fourier coefficients of the eigenstrain. Extracting the average fields — that are associated with $G = 0$ —

¹The number of waves that was found sufficient for convergence in this work is 41, see Appendix A.

from Eq. (16) yields

$$\bar{\mathbf{h}} := \begin{pmatrix} \bar{\boldsymbol{\sigma}} \\ \bar{\mathbf{D}} \\ \bar{\boldsymbol{\rho}} \end{pmatrix} \equiv \begin{pmatrix} \check{\boldsymbol{\sigma}}_0 \\ \check{\mathbf{D}}_0 \\ \check{\boldsymbol{\rho}}_0 \end{pmatrix} = \mathbf{L}_0 \{ \mathbf{J}_0 \bar{\mathbf{w}} - \bar{\mathbf{m}} \} + \mathbf{L}_s \mathbf{J}_s \mathbf{w}_s, \quad (17)$$

where \mathbf{J}_0 and \mathbf{L}_0 are the parts of the matrices that multiply the average fields and $(\circ)_s$ denotes the reduced matrix or vector without the $G = 0$ terms².

Our next step is to express the terms \mathbf{w}_s using $\bar{\mathbf{w}}$ and $\bar{\mathbf{m}}$. To this end, we first write Eq. (15) in the form

$$\mathbf{D}_A^T \mathbf{L}_A (\mathbf{J}_A \mathbf{w}_A - \mathbf{m}_A) = -\mathbf{f}_A. \quad (18)$$

Next, we rewrite Eq. (18) by separating the equations that do not include $G = 0$ and obtain

$$\mathbf{Q}_s \mathbf{w}_s = -\mathbf{T} \{ \mathbf{J}_0 \bar{\mathbf{w}} - \bar{\mathbf{m}} \}, \quad (19)$$

where \mathbf{Q}_s is a square matrix whose entries multiply the average fields, and \mathbf{T} contains the terms of the matrix $\mathbf{D}^T \mathbf{L}$ which multiply the average fields. Next, the fluctuating terms of \mathbf{w} can be expressed using its average value and the material properties, such that

$$\mathbf{w}_s = -\mathbf{Q}_s^{-1} \mathbf{T} \{ \mathbf{J}_0 \bar{\mathbf{w}} - \bar{\mathbf{m}} \}. \quad (20)$$

Substituting Eq. (20) into Eq. (17) yields

$$\bar{\mathbf{h}} = \mathbf{L}_0 \{ \mathbf{J}_0 \bar{\mathbf{w}} - \bar{\mathbf{m}} \} - \mathbf{L}_s \mathbf{J}_s \mathbf{Q}_s^{-1} \mathbf{T} \{ \mathbf{J}_0 \bar{\mathbf{w}} - \bar{\mathbf{m}} \}. \quad (21)$$

We can now identify the effective properties that act on the macroscopic kinematic fields, i.e., on $\{ \mathbf{J}_0 \bar{\mathbf{w}} - \bar{\mathbf{m}} \}$, namely,

$$\begin{pmatrix} \tilde{\mathbf{C}} & \tilde{\mathbf{B}}^\dagger & \tilde{\mathbf{S}} \\ \tilde{\mathbf{B}} & -\tilde{\mathbf{A}} & \tilde{\mathbf{W}} \\ \tilde{\mathbf{S}}^\dagger & \tilde{\mathbf{W}}^\dagger & \tilde{\boldsymbol{\rho}} \end{pmatrix} := \mathbf{L}_0 - \mathbf{L}_s \mathbf{J}_s \mathbf{Q}_s^{-1} \mathbf{T}. \quad (22)$$

The effective properties (22) are of the form reported in Refs. [34, 35, 37]: they are nonlocal in space and time, i.e., functions of $\boldsymbol{\kappa}$ and $\boldsymbol{\omega}$; and include two pairs of adjoint properties—the Willis couplings $\tilde{\mathbf{S}}, \tilde{\mathbf{S}}^\dagger$ and the electromomentum couplings $\tilde{\mathbf{W}}, \tilde{\mathbf{W}}^\dagger$ —which are absent in the microscopic relations. In this work, we focus on maximizing the electromomentum coupling at the long wavelength limit, namely at $\boldsymbol{\kappa} = 0$, in which case $\tilde{\mathbf{S}} = \tilde{\mathbf{S}}^\dagger$ and $\tilde{\mathbf{W}} = \tilde{\mathbf{W}}^\dagger$. We further restrict attention to

²Here \mathbf{L}_0 and \mathbf{L}_s is a 3×3 matrix and a $3 \times (3N - 3)$ matrix, respectively; \mathbf{J}_0 and \mathbf{J}_s is a 3×2 matrix and a $(3N - 3) \times (2N - 2)$ matrix, respectively; $\bar{\mathbf{w}}$ and \mathbf{w}_s is a vector with 2 components and a vector with $2N$, respectively, and $\bar{\mathbf{m}}$ is a vector with 3 components.

the low frequency range, where the electromomentum coefficient is expected to depend linearly on the frequency [34, 36]; Accordingly, we optimize \tilde{W} at 2 kHz. (Indeed, our calculations show that in the range 0 - 10 kHz, \tilde{W} grows linearly with the frequency.) Henceforth, the matrix in Eq. (22) will be denoted by K . In what follows, we analyze K , with the understanding that the component that is relevant to this work is K_{23} .

3 Discrete material choice optimization

We begin by presenting a discrete material choice approach, where the base materials that compose the periodic structure are chosen from a predefined set of available materials given in Table 1. We focus on a laminate made of three constituents, optimize it over the choice of the materials, and evaluate simultaneously the length of each layer that leads to the optimal design, while the total length of the periodic cell is fixed to 3 mm. Thanks to the use of standard base materials, the results of this design parameterization are directly applicable and can contribute significantly to practical implementation. As the optimization is based on discrete variables and the number of design variables is small, a genetic algorithm (GA) is used for solving the optimization problem.

The design variables are assigned to the choice of material in each of the three material layers, from a library of candidate materials, and to the length of each material phase. This corresponds to the maximization problem

$$\begin{aligned}
 & \underset{y_j, l_1, l_2}{\text{maximize}} && |\tilde{W}|, \\
 & \text{subject to} && y_j \in [1, 2, \dots, 10], \quad j = 1, 2, 3, \\
 & && l_1 + l_2 \leq l_T, \\
 & && l_1, l_2 \geq 0,
 \end{aligned} \tag{23}$$

where y_j denotes the pointer to a discrete material that is a member of Table 1. For example, if $y_2 = 3$ then the second layer is Al_2O_3 . The length of the third layer is computed explicitly as the complementary of the total length, hence, it is not considered as a design variable. Note that for each minimal (negative) value of \tilde{W} , there is an equivalent maximal (positive) value of \tilde{W} that can be designed by flipping the order of the structure, since the sign of \tilde{W} depends on the coordinate system [36]. Other operations can also yield equivalent designs with the same absolute value of \tilde{W} , as will be discussed in the next section. Hence, our optimization implementation was to minimize the objective without referring to the absolute value, namely, to obtain the most negative electromomentum coupling.

Material	C [GPa]	ρ [kg/m ³]	B [C/m ²]	A [nF/m]
PZT4	115	7500	15.1	5.6
BaTiO ₃	165	6020	3.64	0.97
Al ₂ O ₃	300	3270	0	0.079
PMMA	3.3	1188	0	0.023
PZT , Navy type II PZT-5H	50	7500	29	30.1
LiNbO ₃	200	4650	1.3	0.25
PMN-PT Single Crystal X2B	100	8100	200	53.1
Quartz	86	2650	0.17	0.04
Soft PZT HK1HD	50	8000	39	60.2
Hard PZT Type I	50	7900	15	11.5

Table 1: The library of candidate materials for the discrete optimization formulation (23).

Number of runs	Minimum confidence required	The calculated confidence
10	0.8	0.8323
20	0.5	0.8326

Table 2: Required and calculated confidence for ending the Genetic Algorithm search.

In general, when using optimization methods, the optimization process might end up with a local minimum instead of a global one, and the outcome can strongly depend on the initial starting point of the whole process. Hence, some form of verification is needed. We define a confidence parameter to determine the threshold for a satisfactory solution. The parameter is computed as follows

$$\begin{aligned}
E &= (E_1 E_2)^{0.5}, \\
E_1 &= \frac{R_{\text{best}}}{R_{\text{total}}}, \\
E_2 &= e^{-2 \frac{E_{\text{avg}} - E_{\text{best}}}{E_{\text{best}}}},
\end{aligned} \tag{24}$$

where multiple runs have been considered; R_{best} is the number of runs that resulted in the optimal solution; R_{total} is the total number of runs; E_{avg} and E_{best} are the average and optimal electro-momentum coupling out of all the outcomes, respectively. The minimum confidence required for ending the search for the optimal design depends on the number of runs, as presented in Table 2, together with the calculated confidence of the process.

Our results show that the optimal structure is 2.052 mm PMN-PT Single Crystal X2B–0.106 mm PMMA–0.842 mm Soft PZT HK1HD, (Figure 2), yielding $\tilde{W} = 6.312 \cdot 10^{-7}$ Cs/m³, which is one order of magnitude larger than the electromomentum coefficient of the reference laminate.

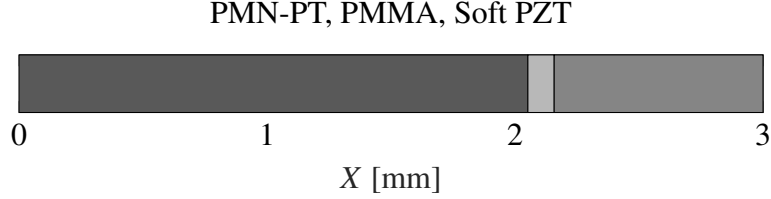


Figure 2: The optimal design according to the discrete material choice approach, found by the GA. Each color represents a different material. The lengths of the layers are 2.052 mm, 0.106 mm and 0.842 mm and $|\tilde{W}| = 6.312 \cdot 10^{-7} \text{ Cs/m}^3$.

We observe that the optimizer provided a laminate with high contrast between the properties of its constituents: PMMA has the smallest value of each one of the electromechanical properties; PMN-PT Single Crystal X2B has the largest piezoelectric coefficient and mass density; PZT HK1HD has the largest dielectric coefficient and second-largest mass density. The asymmetry is not only in the material properties but also in the geometry: the middle layer is very thin with respect to the other two layers. The above features reoccur in subsequent sections.

4 Gradient-based optimization

The efficiency of genetic algorithms strongly depends on the number of design variables, exhibiting a sharp decline when the number of design variables increases. Even though the one-dimensional problem that we address does not require a large number of design variables, the capability to optimize with a large number of variables is desirable in general; for example, in extensions of the current work to higher-dimensional problems. In such cases, gradient-based optimization is more suitable, and this section is dedicated to optimizations using continuous variables that is solved by such gradient-based algorithms. In its most general form, the optimization problem includes design variables that govern the material properties and the geometry of each of the three material phases. An essential building block is the derivation of the analytical sensitivity analysis of the objective function with respect to the design variables, which we carry out in the sequel.

The general problem consists of finding the optimal material properties and the optimal length of each layer. This leads to the following maximization problem

$$\begin{aligned}
 & \underset{z_{mn}, l_1, l_2}{\text{maximize}} && |\tilde{W}|, \\
 & \text{subject to} && l_1 + l_2 \leq l_T, \\
 & && l_1, l_2 \geq 0, \\
 & && z_{mL} \leq z_{mn} \leq z_{mU} \quad \forall m = 1 \dots 4, n = 1 \dots 3,
 \end{aligned} \tag{25}$$

	Upper limits	Lower limits
B [C/m ²]	200	0
A [nF/m]	60.2	0.023
C [GPa]	300	3.3
ρ [kg/m ³]	1188	8100

Table 3: Upper and lower limits for the material properties in Eq. (25).

where z_{mn} denotes the material property m , i.e., B , A , C , ρ , in this order, of layer n . For example, z_{23} is the dielectric coefficient of the third layer. The notation z_{mL} and z_{mU} represents the lower and upper limits of property m . Each material property is optimized independently, thus relaxing the constraint on the relation between the various material properties. The purpose of this FMO [41] is twofold: first, it delivers a theoretical upper bound on the electromomentum coupling; second, it provides guidelines on how to compose a laminate that maximizes \tilde{W} .

In order to obtain results with some correlation to realistic material properties, the design variables are limited in-between the extreme properties among the real materials considered in Section 3, as presented in Table 3. The material properties were normalized with respect to the same limits. The normalized properties are computed as follows

$$\chi_m = \frac{\chi_{phys} - \chi_L}{\chi_U - \chi_L}, \quad (26)$$

where χ_m and χ_{phys} are the normalized and the physical property, respectively; and χ_L and χ_U are the lower and upper limits, respectively.

4.1 Sensitivity analysis

We carry out a differentiation of the objective function with respect to each one of the design variables, i.e., the lengths of the first two layers and the material properties of each layer. Considering first the length variables, the derivative of Eq. (22) using the product rule yields

$$\frac{\partial \mathcal{K}}{\partial l_n} = - \left[\frac{\partial \mathbf{L}_s}{\partial l_n} \mathbf{J}_s \mathbf{Q}_s^{-1} \mathbf{T} + \mathbf{L}_s \mathbf{J}_s \frac{\partial \mathbf{Q}_s^{-1}}{\partial l_n} \mathbf{T} + \mathbf{L}_s \mathbf{J}_s \mathbf{Q}_s^{-1} \frac{\partial \mathbf{T}}{\partial l_n} \right]. \quad (27)$$

Since the PWE expands the governing- and constitutive equations in Fourier series, the entries in each matrix listed in Eq. (27) are basically Fourier coefficients, as given in Eq. (8). Thus, differentiating $\check{\xi}_G$ and following the same procedure yields the derivatives that we are looking for, namely $\frac{\partial \mathbf{L}_s}{\partial l_n}$, $\frac{\partial \mathbf{Q}_s}{\partial l_n}$ and $\frac{\partial \mathbf{T}}{\partial l_n}$. Since we are analyzing trilayer laminates, the integral is divided into three

parts, namely,

$$\check{\xi}_G = l_T^{-1} \left[\int_0^{l_1} \xi_1 e^{-iGx} dx + \int_{l_1}^{l_2} \xi_2 e^{-iGx} dx + \int_{l_2}^{l_3} \xi_3 e^{-iGx} dx \right]. \quad (28)$$

Then, following the product rule, the derivative is expressed as

$$\frac{\partial \check{\xi}_G}{\partial l_1} = \frac{1}{l_T} \left\{ \xi_1 e^{-iG(l_1)} + \xi_2 \left[e^{-iG(l_1+l_2)} - e^{-iG(l_1)} \right] + \xi_3 \left[e^{-iG(l_1+l_2+l_3)} - e^{-iG(l_1+l_2)} \right] \right\}, \quad (29)$$

$$\frac{\partial \check{\xi}_G}{\partial l_2} = \frac{1}{l_T} \left\{ \xi_2 e^{-iG(l_1+l_2)} + \xi_3 \left[e^{-iG(l_1+l_2+l_3)} - e^{-iG(l_1+l_2)} \right] \right\}, \quad (30)$$

$$\frac{\partial \check{\xi}_G}{\partial l_3} = \frac{1}{l_T} \left\{ \xi_3 e^{-iG(l_1+l_2+l_3)} \right\}. \quad (31)$$

The chain rule yields

$$\frac{d(\cdot)}{dl_j} = \frac{\partial(\cdot)}{\partial l_j} + \frac{\partial(\cdot)}{\partial l_3} \frac{\partial l_3}{\partial l_j}, \quad j = 1, 2, \quad (32)$$

and we recall that total length of the periodic cell is fixed, hence

$$\frac{d(\cdot)}{dl_j} = \frac{\partial(\cdot)}{\partial l_j} - \frac{\partial(\cdot)}{\partial l_3}, \quad (33)$$

where (\cdot) denotes the matrices L_s , Q_s and T . Now that we have the derivatives above, we can follow the same process as described in Section 2, and obtain the desired derivatives in the same manner as in computing L_s , Q_s and T . Note that according to Eq. (27), one must compute the derivative of Q_s^{-1} , and this is carried out using the relation

$$\frac{\partial Q_s^{-1}}{\partial l_j} = -Q_s^{-1} \cdot \frac{\partial Q_s}{\partial l_j} \cdot Q_s^{-1}. \quad (34)$$

The sensitivities with respect to material properties are derived similarly to the procedure outlined above for the length variables. Analogously to Eq. (27), the sensitivity with respect to any material property is expressed as

$$\frac{\partial K}{\partial z_{mn}} = - \left[\frac{\partial L_s}{\partial z_{mn}} J_s Q_s^{-1} T + L_s J_s \frac{\partial Q_s^{-1}}{\partial z_{mn}} T + L_s J_s Q_s^{-1} \frac{\partial T}{\partial z_{mn}} \right]. \quad (35)$$

Again, the entries of the matrices are Fourier coefficients, therefore the derivative of Eq. (28) with

respect to the material properties is

$$\frac{\partial \check{\xi}_G}{\partial z_{m1}} = \frac{-1}{iGl_T} \left[e^{-iG(l_1)} - 1 \right], \quad (36)$$

$$\frac{\partial \check{\xi}_G}{\partial z_{m2}} = \frac{-1}{iGl_T} \left[e^{-iG(l_1+l_2)} - e^{-iGl_1} \right], \quad (37)$$

$$\frac{\partial \check{\xi}_G}{\partial z_{m3}} = \frac{-1}{iGl_T} \left[e^{-iG(l_1+l_2+l_3)} - e^{-iG(l_1+l_2)} \right]. \quad (38)$$

Henceforth, a procedure analogous to the PWE is carried out to obtain the required sensitivities, namely $\frac{\partial L_s}{\partial z_{mn}}$, $\frac{\partial Q_s}{\partial z_{mn}}$ and $\frac{\partial T}{\partial z_{mn}}$. Note that we have compared the evaluation of the analytical expressions for the derivatives with numerical derivatives that were obtained by finite differences. This comparison yielded an excellent agreement, thereby verifying the correctness of our sensitivity analysis.

4.2 Test case: optimization over the lengths

We begin our numerical investigation with a benchmark problem of length optimization; this simple problem allows us to graphically verify our optimization method.

We consider two triplets of materials. The first triplet consists of the materials PZT4, BaTiO₃ and Al₂O₃. The graphical solution is presented in Figure 3a, where we observe that the optimal design is located near the diagonal. This means that the third layer should be thin in order to maximize the absolute value of \tilde{W} , which is found to be $8.462 \cdot 10^{-9}$ Cs/m³. Solving the problem by a numerical optimization scheme using the method of moving asymptotes [59], we obtain the same result with the iterative convergence as plotted in Figure 3b. The optimal solution is characterized by the material distribution of $l_1 = 1.38$ mm, $l_2 = 1.28$ mm and $l_3 = 0.3979$ mm.

The second triplet consists of the materials Al₂O₃, BaTiO₃ and PMMA, which corresponds to the reference laminate when all layers have the same length. Figure 3c shows the graphical solution, where we observe that the optimal design is located near the diagonal. The gradient-based optimization achieves the same result, $\tilde{W} = 9.52 \cdot 10^{-9}$ Cs/m³, as indicated in Figure 3d, which shows the iterative convergence of the gradient-based optimization. This result reflects a fourfold improvement with respect to the reference laminate, achieved solely by changing its geometry. Specifically, this optimal design is the lengths $l_1 = 0.69$ mm, $l_2 = 2.13$ mm and $l_3 = 0.19$ mm, for layers one to three, respectively. Both results are summarized in Table 4. We observe that the optimal designs share a common feature: a thin layer with the lowest mass density and piezoelectric coefficient. This is a repeating feature throughout the following optimization problems.

The graphical solution in Figure 3c shows that the optimization problem with this set of materials exhibits several local minima. Using a gradient-based method, this might lead to results that

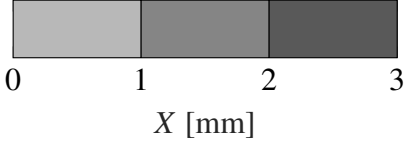
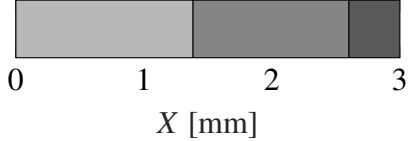
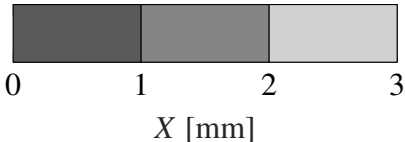
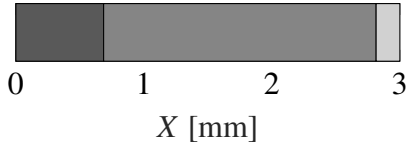
Composition	\tilde{W} : Equally divided design [Cs/m ³]	\tilde{W} : Optimal design [Cs/m ³]
PZT4-BaTiO ₃ -Al ₂ O ₃	$\tilde{W} = -5.88 \cdot 10^{-9}$	$\tilde{W} = -8.46 \cdot 10^{-9}$
		
Al ₂ O ₃ -BaTiO ₃ -PMMA	$\tilde{W} = -2.34 \cdot 10^{-9}$	$\tilde{W} = 9.52 \cdot 10^{-9}$
		

Table 4: Results of length optimization using gradient-based optimization. The optimal lengths of the layers in the first composition are 1.38 mm, 1.28 mm and 0.3979 mm, and for the second composition they are 0.69 mm, 2.13 mm and 0.19 mm. Each color represents a different material. Both optimal designs exhibit a structure with one relatively thin layer.

depend heavily on the initial structure. In order to overcome this problem, the optimization process has been divided into two steps. The first step seeks the optimal region by calculating the objective function at 20 random points inside the feasible region. Once the best starting point is found, in the second step we use the gradient-based optimization to steer the design towards a nearby minimum point.

As inferred from Eq. (25), the length of the third layer is not a design variable. This may hamper convergence because the maximum change in the length of the third layer is related to the design variables, which are the lengths of the two other layers. For example, in cases where the optimal solution is located near the diagonal, the length of the third layer is small compared to the first and the second layers. Then a design change that is suitable for the design variables, might be too liberal for the third layer and divergence may occur. Therefore, conservative values of a move limit on the change of the design variables were imposed. In all examples, a maximum move limit of 0.03 mm was enforced.

4.3 Optimization over different material properties

Having verified our gradient-based optimization using a test case, we proceed to investigate optimization problems whose design variables are chosen material properties, where the rest of the properties are set to the properties of Navy type II PZT-5H.

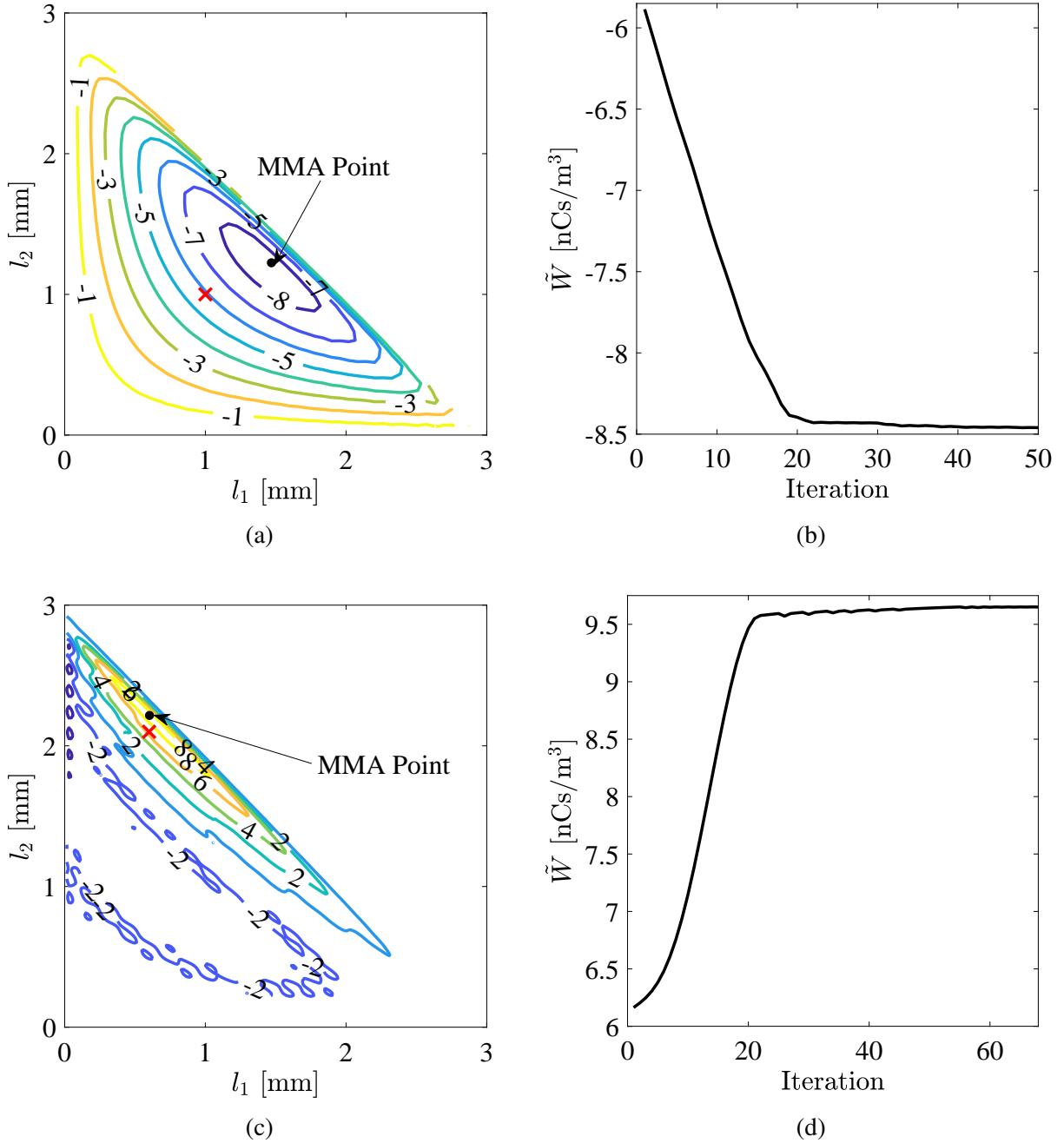


Figure 3: Results of the length optimization. Panels (a) and (b) present the optimal solution for the first composition: (a) Graphical solution; (b) Convergence of the gradient-based optimization. Panels (c) and (d) present the optimal solution for the second composition: (c) Graphical solution; (d) Convergence of the gradient-based optimization. In both contours the initial (optimal) design is marked with red cross (black dot), and the objective function is multiplied by 10^9 .

We begin by considering the design space of the piezoelectric coefficient and mass density of each layer, yielding six design variables. For this case, the optimal electromomentum coefficient

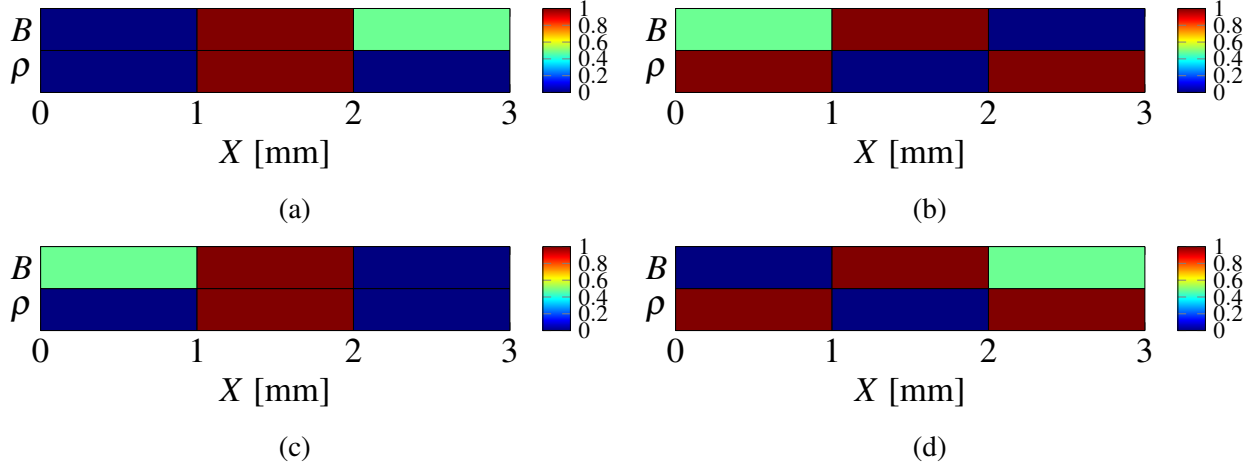


Figure 4: Four equivalent optimal designs as an outcome of the FMO over the piezoelectric and the mass density properties. Panels (a) and (b) share the same sign of the electromomentum coupling, while panels (c) and (d) have the opposite sign with the same magnitude. The properties were color-scaled as yellow (blue) color denotes the upper (lower) limit value. The optimal $|\tilde{W}|$ for all four designs is $5.687 \cdot 10^{-6} \text{ Cs/m}^3$.

is $5.687 \cdot 10^{-6} \text{ Cs/m}^3$, which is three orders of magnitude greater than that of the reference laminate. This value is achieved by four equivalent designs, as displayed in Figure 4; the properties were color-scaled as yellow (blue) color denotes the upper (lower) limit value. The same color scaling will be used in the subsequent results. The optimal design exhibits a large contrast between the material properties, as 5 out of 6 properties attain the limit values, and one remaining piezoelectric coefficient attains the intermediate value 96.25 C/m^2 . This result qualitatively agrees with the insights of Pernas-Salomón et al. [36], who carried out heuristic homogenization of a single trilayer piezoelectric element, based on its scattering properties. Specifically, Eq. (41f) therein suggests that the electromomentum coefficient depends on the contrast of B/A between the layers, with some weight that depends on the rest of the properties. Accordingly, it appears that the optimal laminates maximize the contrast between the two layers which have the largest weight function.

The four optimal designs are similar to each other: the mapping from one optimal design to another is obtained by swapping the first and the third layer, and/or flipping the contrast of the mass density. This means that layers with minimal mass density are replaced with maximal mass density and vice versa; layers with maximal mass density are replaced with minimal mass density. We refer to this transformation as the *flipping* of ρ . Each of the two transformation steps alone flips the sign of \tilde{W} .

We demonstrate these two transformations using the laminates in Figure 4a and in Figure 4d, that share the same arrangement of the piezoelectric coefficient, but flipped values of the mass density, leading to the same magnitude with opposite sign of the electromomentum coefficient. The laminates in Figure 4a and Figure 4b have the mirrored arrangement of B and also flipped

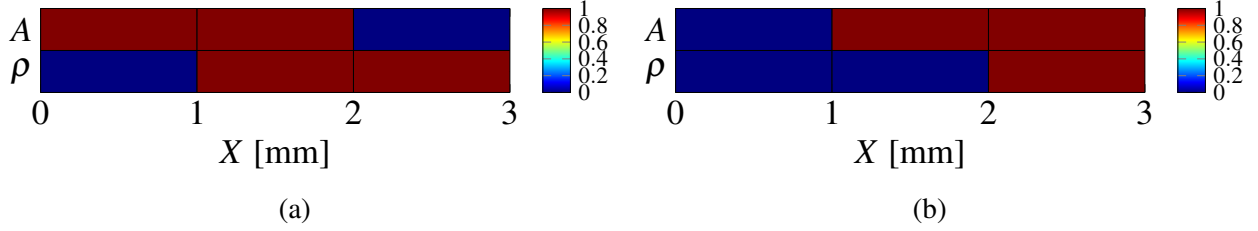


Figure 5: Free material optimization over the dielectric and the mass density properties. Panels (a) and (b) show two equivalent optimal designs, where the properties were color-scaled as yellow (blue) color denotes the upper (lower) limit value, and the optimal $|\tilde{W}|$ is $4.516 \cdot 10^{-6}$ Cs/m³.

values of ρ , leading to the same value of \tilde{W} .

These observations correspond to the direction-dependent response of the medium [36], captured by the anisotropic nature of \tilde{W} . As noted by Pernas-Salomon et al. [36], \tilde{W} flips sign when the coordinate system is reversed, which is equivalent to the inversion of the unit cell.

Our second case study optimizes over the mass density and dielectric coefficient. We find four designs, two of which are displayed in Figure 5, which are related through the transformations mentioned earlier. The optimal coefficient is $4.516 \cdot 10^{-6}$, which is smaller than the coefficient that was obtained when optimizing over ρ and B , yet it is still three order of magnitude larger than that of the reference laminate. Interestingly, here all six properties attain limiting values, not only five as in the optimization over ρ and B , i.e., the dependency of \tilde{W} on A is different from its dependency on B .

The last optimization problem considers all these three material properties, i.e., A, B and ρ , as design variables. Figure 6 presents two optimal and equivalent designs of the design variables. Again, the mass density and dielectric coefficient of all the layers attain the limiting value, as well as the piezoelectric coefficient of two out of the three layers. The resultant electromomentum coefficient is larger by an additional order of magnitude, in comparison with the coefficient that was obtained when only pairs of material properties were optimized.

Finally, we report that additional computations (not shown here) with ρ or B/A as prescribed constant values in the unit cell, lead to zero \tilde{W} , regardless of the design variables chosen. The fact that constant B/A yields zero \tilde{W} is in agreement with the results of Pernas-Salomón et al. [36]. However, Eq. (41f) in the latter reference, which we recall is based on the homogenization of a single scatterer, implies that \tilde{W} can be nonzero with constant ρ , a result that is different from our current calculations, which are based on homogenization of periodic media.

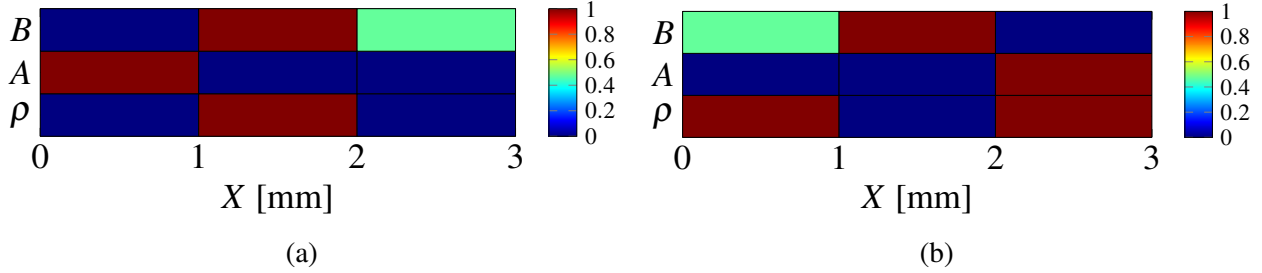


Figure 6: Free material optimization over the piezoelectric, the dielectric and the mass density properties. Panels (a) and (b) show two equivalent optimal designs, where the properties were color-scaled as yellow (blue) color denotes the upper (lower) limit value, and the optimal $|\tilde{W}|$ is $1.0354 \cdot 10^{-5} \text{ Cs/m}^3$.

4.4 Complete free material optimization

Figure 7a presents the hypothetical optimal design that is obtained by removing all design restrictions. Accordingly, the design variables are the four material properties and the length of the layers. The resultant electromomentum coefficient is $5.7 \cdot 10^{-5} \text{ Cs/m}^3$, which is fourfold the coefficient that was obtained when the optimization was over the triplet ρ, A and B . All the material properties attain the limiting values, except the piezoelectric coefficient of one single layer. Interestingly, the optimal stiffness is constant in the cell, the value of which is the lower limit, corresponding to a soft laminate. The optimal lengths yield a thin layer (volume fraction of 11%), in-between two thick layers (volume fractions of 47% and 42%). This result resembles the one that we obtained in the length optimization problem. Note that, again, equivalent designs can be obtained by mirroring the periodic cell and/or flipping the mass density values. Such equivalent design is shown in Figure 7b.

Interestingly, the optimization process not only increases \tilde{W} , but also increases the relative contribution of both the electromomentum and the Willis effects to the effective linear momentum. To show this, we compare in Figure 7c the momentum ratios $\frac{\tilde{S}\langle u_x \rangle}{\tilde{\rho}\langle u_t \rangle}$ (solid lines) and $\frac{\tilde{W}\langle \phi_x \rangle}{\tilde{\rho}\langle u_t \rangle}$ (dashed lines), in the reference laminate (blue lines) and the FMO design-based laminate (black lines), as functions of the frequency. (The reader is referred to Appendix C in the Ref. [34] for details in the calculations of $\langle u_t \rangle$ and $\langle \phi_x \rangle$.) We also observe that while $\tilde{W}\langle \phi_x \rangle$ in the reference laminate is negligible with respect to $\tilde{S}\langle u_t \rangle$, it surpasses $\tilde{S}\langle u_t \rangle$ in the optimized laminate.

To quantify the contribution of the geometrical variables to the optimization, we optimize next only over the four material properties, keeping the length of each layer fixed and equal to 1 mm. The resultant electromomentum coefficient is $4.192 \cdot 10^{-5} \text{ Cs/m}^3$. This value is about 71% of the coefficient that was obtained when the geometrical and material parameters were included in the design space. Two of the equivalent, optimal designs are displayed in Figure 8. These laminates are different from those that were obtained so far, as none of the layers exhibits a maximal piezoelectric coefficient.

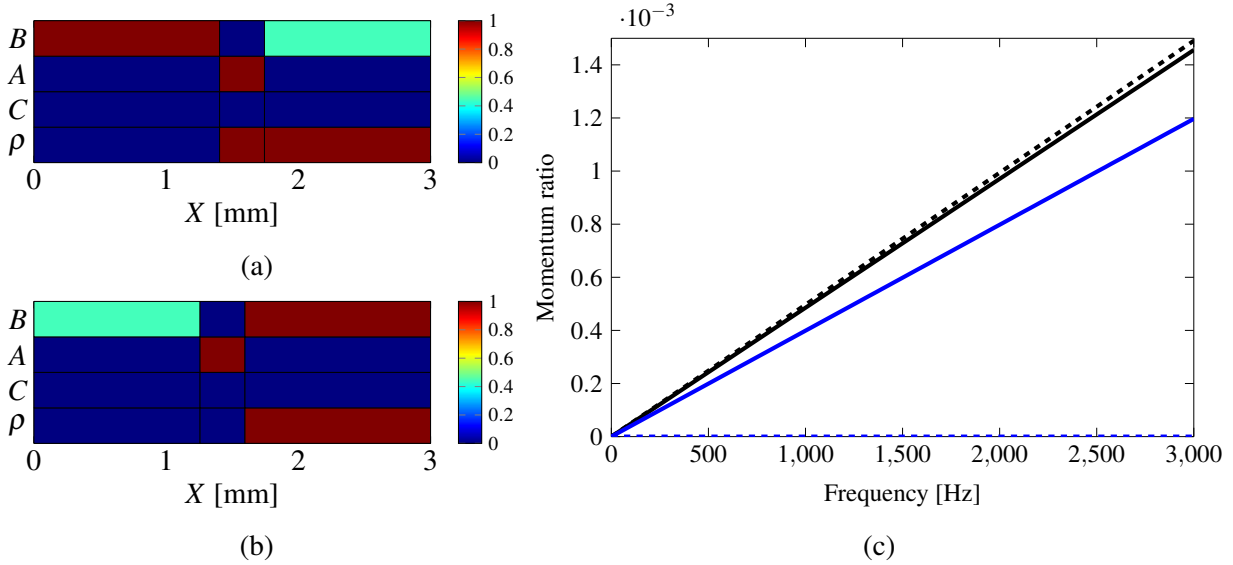


Figure 7: Free material optimization over all the material and geometric properties. Panels (a) and (b) show two equivalent optimal designs, where the properties were color-scaled as yellow (blue) color denotes the upper (lower) limit value, and the optimal $|\tilde{W}|$ is $5.7 \cdot 10^{-5}$ Cs/m³. Panel (c) displays the momentum ratios of the off-diagonal couplings: Solid blue (black) curve represents the Willis momentum ratio, namely, $\frac{\tilde{S}\langle u_x \rangle}{\tilde{\rho}\langle u_t \rangle}$ for the reference laminate (FMO optimal design), and dashed blue (black) curve denotes the electromomentum coupling momentum ratio, namely, $\frac{\tilde{W}\langle \phi_x \rangle}{\tilde{\rho}\langle u_t \rangle}$ for the reference laminate (FMO optimal design).

4.5 Optimization over the designable mass density and stiffness

The results of the previous section provide a hypothetical upper bound for the electromomentum coefficient, which is accessible only if all material properties can be engineered independently. The significant progress on the design of engineered stiffness and mass density [60, 61], motivates us to term the optimal design of C and ρ as the applicable design. Figure 9 shows the solution of this optimization over C and ρ , when the rest of the properties are chosen according to the DMO optimal result (Figure 2). The resultant electromomentum coefficient is $1.282 \cdot 10^{-6}$ Cs/m³, which is only one order of magnitude lower than the hypothetical upper bound. Here again, the optimization process delivers a constant minimal stiffness, and maximizes the contrast of ρ in the cell, as it attains the lowest limit in layers two and three, and the upper limit in layer one.

A summary of the optimal electromomentum coefficients, together with the reference laminate and the improvement relatively to it, is given in Table 5.

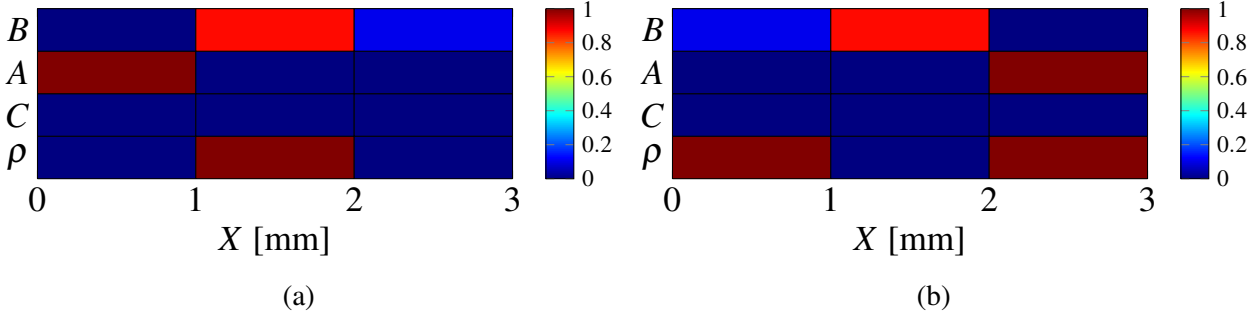


Figure 8: Free material optimization over all the material properties with the length held fixed. Panels (a) and (b) show two equivalent optimal designs, where the properties were color-scaled as yellow (blue) color denotes the upper (lower) limit value, and the optimal $|\tilde{W}|$ is $4.192 \cdot 10^{-5} \text{ Cs/m}^3$.

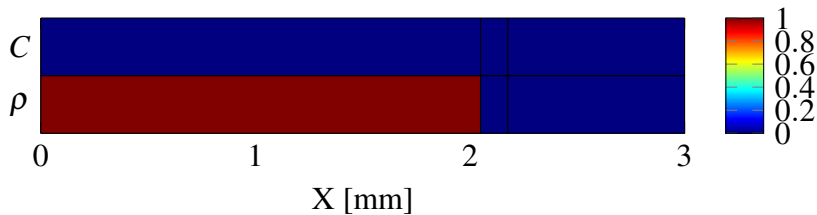


Figure 9: Optimization over the designable mass density and stiffness. The optimal design is the result of optimizing the composition of the DMO optimal result (Figure 2) over continuous mass density, stiffness and length. The lengths of the laminates are 2.0489 mm, 0.1273 mm and 0.8238 mm. The properties were color-scaled as yellow (blue) color denotes the upper (lower) limit value. The optimal objective is $1.282 \cdot 10^{-6} \text{ Cs/m}^3$.

5 Summary

A prominent challenge in engineering today is to control elastic waves; metamaterials exhibiting the electromomentum effect [34] offer a way to tune the phase velocity and generate asymmetry in the phase angle of such waves [34, 36]. To make these phenomena more pronounced, it is required to design these metamaterials with large electromomentum coefficient. In this work, we have utilized discrete material-, topology- and free material optimization methods to maximize the electromomentum coupling of periodic piezoelectric trilayer laminates in the low frequency, long-wavelength limit. These optimization methods are essentially inverse homogenization methods, since we have formulated the objective function, namely, the electromomentum coefficient, as the end result of a rigorous homogenization process [34, 37].

The discrete material optimization, which uses a predefined set of real materials as its design space, has yielded an electromomentum coefficient that is two orders of magnitude larger than the arbitrary laminate that was first analyzed by Pernas-Salomón and Shmuel [34]. We observed that the optimization yields a choice of materials that tends to maximize the contrast between their electromechanical properties, in a unit cell that comprises one thin layer in-between two thick

	$ \tilde{W} $ [Cs/m ³]	Relative improvement ratio
The reference laminate	$2.342 \cdot 10^{-9}$	-
DMO	$6.312 \cdot 10^{-7}$	269.51
Length optimization	$9.52 \cdot 10^{-9}$	4.06
FMO: B and ρ	$5.687 \cdot 10^{-6}$	2428.26
FMO: A and ρ	$4.516 \cdot 10^{-6}$	1928.27
FMO: B, A and ρ	$1.0354 \cdot 10^{-5}$	4421.01
FMO: all properties	$4.192 \cdot 10^{-5}$	17899.23
FMO: all properties and length	$5.7 \cdot 10^{-5}$	24338.17
Synthesizing C and ρ	$1.282 \cdot 10^{-6}$	547.40

Table 5: The electromomentum coefficient of the reference laminate (equispaced Al₂O₃, BaTiO₃ and PMMA layers); the optimal laminates that were reported in this work, and the relative improvement with respect to the reference laminate coefficient.

layers.

The free material optimization uses a design space with continuous variables, the values of which are bounded in-between the extreme values of the materials considered earlier. We have employed gradient-based algorithms that were implemented together with a sensitivity analysis of the objective function. Using these algorithms, we have solved optimization problems whose design variables are pairs of the mass density and one of the electromechanical properties: the dielectric-, piezoelectric- or stiffness coefficients. The rest of the properties were set to the properties of the reference laminate. We have found that the optimal values of each one of these pairs enlarge the electromomentum coefficient by another order of magnitude, in comparison with the optimal laminate that the discrete material optimization delivered. We observed that the pair that demonstrated the best improvement was with the piezoelectric coefficient. We further found that when all material properties are designable, the electromomentum coefficient is enlarged by another order of magnitude.

The optimal laminates reveal how the electromomentum depends on the contrast in the electromechanical properties between the layers. Specifically, we observed that the optimization tends to maximize the electromechanical properties in certain layers, and minimize the same properties in the remaining layers. Two exceptions are the piezoelectric coefficient, which, while tending to the two extreme values in two layers, tends to an intermediate value at the remaining layer; and the stiffness, which the optimization minimizes throughout the whole cell. The optimal laminates also show that the geometry that maximizes the electromomentum coefficient is of a thin layer, in-between two thick layers.

Collectively, our results provide guidelines for the design of metamaterials with maximum electromomentum coefficient, paving the way for future work on their integration in wave control ap-

plications.

Acknowledgments

The authors wish to thank Alon Landmann for providing the controls over convergence of GA in Eq. (24). This research was supported by the Ministry of Science and Technology, Israel (Grant no. 880011), and by the Israel Science Foundation, funded by the Israel Academy of Sciences and Humanities (Grant no. 2061/20).

Appendices

A The convergence of the PWE method

To examine the convergence of the method, the electromomentum coupling was evaluated for a combination of three fixed materials. Results show convergence at 30 Fourier waves, as shown in Figure 10. Moreover, to examine the rate of convergence, three different divisions were considered; one is equally divided, one with one short layer compared to the other two layers and the third is the average of the previous two. As expected, the higher the contrast between the length of each layer, the slower the rate of convergence of the method.

B Detailed expressions for the matrices in the PWE method

The matrices can be divided into sub-matrices following

$$\begin{aligned}
 \mathbf{L}_A &= \begin{pmatrix} \mathbf{L}^{(1,1)} & \mathbf{L}^{(1,2)} & \mathbf{L}^{(1,3)} \\ \mathbf{L}^{(2,1)} & \mathbf{L}^{(2,2)} & \mathbf{L}^{(2,3)} \\ \mathbf{L}^{(3,1)} & \mathbf{L}^{(3,2)} & \mathbf{L}^{(3,3)} \end{pmatrix}, \mathbf{D}_A = \begin{pmatrix} \mathbf{D}^{(1,1)} & \mathbf{D}^{(1,2)} \\ \mathbf{D}^{(2,1)} & \mathbf{D}^{(2,2)} \\ \mathbf{D}^{(3,1)} & \mathbf{D}^{(3,2)} \end{pmatrix}^T, \mathbf{h}_A = \begin{pmatrix} \mathbf{h}^{(1)} \\ \mathbf{h}^{(2)} \\ \mathbf{h}^{(3)} \end{pmatrix}, \\
 \mathbf{J}_A &= \begin{pmatrix} \mathbf{J}^{(1,1)} & \mathbf{J}^{(1,2)} \\ \mathbf{J}^{(2,1)} & \mathbf{J}^{(2,2)} \\ \mathbf{J}^{(3,1)} & \mathbf{J}^{(3,2)} \end{pmatrix}, \mathbf{w}_A = \begin{pmatrix} \mathbf{w}^{(1)} \\ \mathbf{w}^{(2)} \end{pmatrix}, \mathbf{m}_A = \begin{pmatrix} \mathbf{m}^{(1)} \\ \mathbf{m}^{(2)} \\ \mathbf{m}^{(3)} \end{pmatrix}, \mathbf{f}_A = \begin{pmatrix} \mathbf{f}^{(1)} \\ \mathbf{f}^{(2)} \end{pmatrix},
 \end{aligned} \tag{39}$$

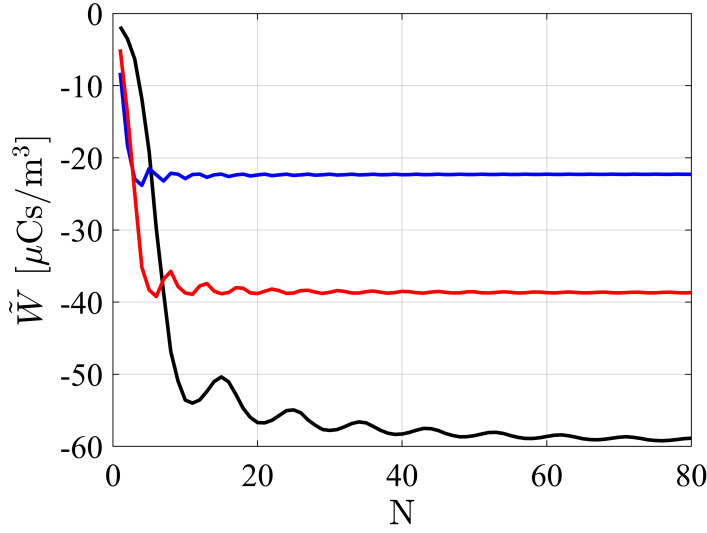


Figure 10: The electromomentum coupling versus the number of Fourier waves used. The black, red and blue curves denote the high, medium and low contrast structures, respectively. The three curves show convergence at $N = 35$.

where the components of the matrix L_A are simply a sub-matrices of the material properties, namely

$$\begin{aligned}
L_{GG'}^{(1,1)} &= \check{C}_{GG'}, L_{GG'}^{(1,2)} = \check{B}_{GG'}, \\
L_{GG'}^{(2,1)} &= \check{B}_{GG'}, L_{GG'}^{(2,2)} = -\check{A}_{GG'}, \\
L_{GG'}^{(3,3)} &= \check{\rho}_{GG'}, L_{GG'}^{(1,3)} = L_{GG'}^{(2,3)} = L_{GG'}^{(3,1)} = L_{GG'}^{(3,2)} = \check{\theta}_{GG'},
\end{aligned} \tag{40}$$

and as has been mentioned before, D_A is composed of three diagonal matrices and three zero matrices, namely

$$\begin{aligned}
D_{GG'}^{(1,1)} &= D_{GG'}^{(2,2)} = \check{\delta}_{GG'} i(\kappa + G), \\
D_{GG'}^{(3,1)} &= \check{\delta}_{GG'} i\omega, \\
D_{GG'}^{(1,2)} &= D_{GG'}^{(2,1)} = D_{GG'}^{(3,2)} = \check{\theta}_{GG'},
\end{aligned} \tag{41}$$

in the same manner, J_A is in the form

$$\begin{aligned}
J_{GG'}^{(1,1)} &= J_{GG'}^{(2,2)} = \check{\delta}_{GG'} i(\kappa + G'), \\
J_{GG'}^{(3,1)} &= -\check{\delta}_{GG'} i\omega, \\
J_{GG'}^{(1,2)} &= J_{GG'}^{(2,1)} = J_{GG'}^{(3,2)} = \check{\theta}_{GG'}.
\end{aligned} \tag{42}$$

The description of the vectors is similar, where h_A is

$$h_G^{(1)} = \check{\sigma}_G, \quad h_G^{(2)} = \check{D}_G, \quad h_G^{(3)} = \check{p}_G, \tag{43}$$

and w_A

$$w_{G'}^{(1)} = \check{u}_{G'}, \quad w_{G'}^{(2)} = \check{\phi}_{G'}, \quad (44)$$

and f_A definitely

$$f_G^{(1)} = \check{f}_G, \quad f_G^{(2)} = -\check{q}_G, \quad (45)$$

and for m_A

$$m^{(1)} = \check{\eta}_G, \quad m^{(2)} = 0, m^{(3)} = 0. \quad (46)$$

References

- [1] Muamer Kadic, Graeme W. Milton, Martin van Hecke, and Martin Wegener. 3d metamaterials. *Nature Reviews Physics*, 1(3):198–210, 2019. doi: 10.1038/s42254-018-0018-y. URL <https://doi.org/10.1038/s42254-018-0018-y>.
- [2] Johan Christensen, Muamer Kadic, Oliver Kraft, and Martin Wegener. Vibrant times for mechanical metamaterials. *MRS Communications*, 5:453–462, 2015. doi: 10.1557/mrc.2015.51.
- [3] Richard V Craster and Sébastien Guenneau. *Acoustic metamaterials: Negative refraction, imaging, lensing and cloaking*, volume 166. Springer Science & Business Media, 2012.
- [4] Pierre A Deymier. *Acoustic metamaterials and phononic crystals*, volume 173. Springer Science & Business Media, 2013.
- [5] G Ma and P Sheng. Acoustic metamaterials: From local resonances to broad horizons. *Sci. Adv.*, 2(2), 2016. doi: 10.1126/sciadv.1501595. URL <http://advances.sciencemag.org/content/2/2/e1501595>.
- [6] C. R. Simovski. Material parameters of metamaterials (a review). *Optics and Spectroscopy*, 107(5):726, 2009. doi: 10.1134/S0030400X09110101. URL <https://doi.org/10.1134/S0030400X09110101>.
- [7] David R. Smith and John B. Pendry. Homogenization of metamaterials by field averaging (invited paper). *J. Opt. Soc. Am. B*, 23(3):391–403, Mar 2006. doi: 10.1364/JOSAB.23.000391. URL <http://josab.osa.org/abstract.cfm?URI=josab-23-3-391>.
- [8] Ben Lustig, Guy Elbaz, Alan Muhafra, and Gal Shmuel. Anomalous energy transport in laminates with exceptional points. *Journal of the Mechanics and Physics of Solids*, page 103719, 2019. ISSN 0022-5096. doi: <https://doi.org/10.1016/j.jmps.2019.103719>. URL <http://www.sciencedirect.com/science/article/pii/S0022509619306921>.
- [9] A Sridhar, V G Kouznetsova, and M G D Geers. A general multiscale framework for the emergent effective elastodynamics of metamaterials. *J. Mech. Phys. Solids*, 111:414–433, 2018. ISSN 0022-5096. doi: <https://doi.org/10.1016/j.jmps.2017.11.017>. URL <http://www.sciencedirect.com/science/article/pii/S0022509617306245>.
- [10] Martin Wegener. Metamaterials beyond optics. *Science*, 342(6161):939–940, 2013. ISSN 0036-8075. doi: 10.1126/science.1246545. URL <https://science.sciencemag.org/content/342/6161/939>.

- [11] J R Willis. The nonlocal influence of density variations in a composite. *Int. J. Solids Struct.*, 21(7):805–817, 1985. ISSN 0020-7683. doi: [https://doi.org/10.1016/0020-7683\(85\)90084-8](https://doi.org/10.1016/0020-7683(85)90084-8). URL <http://www.sciencedirect.com/science/article/pii/0020768385900848>.
- [12] J R Willis. Variational principles for dynamic problems for inhomogeneous elastic media. *Wave Motion*, 3(1):1–11, 1981. ISSN 0165-2125. doi: [https://doi.org/10.1016/0165-2125\(81\)90008-1](https://doi.org/10.1016/0165-2125(81)90008-1). URL <http://www.sciencedirect.com/science/article/pii/0165212581900081>.
- [13] John R Willis. Variational and related methods for the overall properties of composites. *Advances in applied mechanics*, 21:1–78, 1981.
- [14] Shixu Meng and Bojan B Guzina. On the dynamic homogenization of periodic media: Willis’ approach versus two-scale paradigm. *Proc. R. Soc. London A Math. Phys. Eng. Sci.*, 474(2213), 2018. ISSN 1364-5021. doi: 10.1098/rspa.2017.0638. URL <http://rspa.royalsocietypublishing.org/content/474/2213/20170638>.
- [15] G W Milton and J R Willis. On modifications of Newton’s second law and linear continuum elastodynamics. *Proc. R. Soc. London A Math. Phys. Eng. Sci.*, 463(2079):855–880, 2007. ISSN 1364-5021. doi: 10.1098/rspa.2006.1795. URL <http://rspa.royalsocietypublishing.org/content/463/2079/855>.
- [16] Michael B Muhlestein, Caleb F Sieck, Andrea Alù, and Michael R Haberman. Reciprocity, passivity and causality in Willis materials. *Proc. R. Soc. London A Math. Phys. Eng. Sci.*, 472(2194), 2016. ISSN 1364-5021. doi: 10.1098/rspa.2016.0604. URL <http://rspa.royalsocietypublishing.org/content/472/2194/20160604>.
- [17] Hussein Nassar, Qi-Chang He, and Nicolas Auffray. Willis elastodynamic homogenization theory revisited for periodic media. *Journal of the Mechanics and Physics of Solids*, 2015.
- [18] A N Norris, A L Shuvalov, and A A Kutsenko. Analytical formulation of three-dimensional dynamic homogenization for periodic elastic systems. *Proc. R. Soc. London A Math. Phys. Eng. Sci.*, 2012. ISSN 1364-5021. doi: 10.1098/rspa.2011.0698. URL <http://rspa.royalsocietypublishing.org/content/early/2012/02/14/rspa.2011.0698>.
- [19] Li Quan, Younes Ra’di, Dimitrios L Sounas, and Andrea Alù. Maximum Willis Coupling in Acoustic Scatterers. *Phys. Rev. Lett.*, 120(25):254301, 2018. doi: 10.1103/PhysRevLett.

120.254301. URL <https://link.aps.org/doi/10.1103/PhysRevLett.120.254301>.

- [20] A. L. Shuvalov, A. A. Kutsenko, A. N. Norris, and O Poncelet. Effective Willis constitutive equations for periodically stratified anisotropic elastic media. *Proc. R. Soc. London A Math. Phys. Eng. Sci.*, 467(2130):1749–1769, 2011. ISSN 1364-5021. doi: 10.1098/rspa.2010.0389. URL <http://rspa.royalsocietypublishing.org/content/467/2130/1749>.
- [21] Caleb F Sieck, Andrea Alù, and Michael R Haberman. Origins of Willis coupling and acoustic bianisotropy in acoustic metamaterials through source-driven homogenization. *Phys. Rev. B*, 96(10):104303, 2017. doi: 10.1103/PhysRevB.96.104303. URL <https://link.aps.org/doi/10.1103/PhysRevB.96.104303>.
- [22] Ankit Srivastava. Causality and passivity in elastodynamics. *Proceedings of the Royal Society of London A: Mathematical, Physical and Engineering Sciences*, 471(2180), 2015. ISSN 1364-5021. doi: 10.1098/rspa.2015.0256. URL <http://rspa.royalsocietypublishing.org/content/471/2180/20150256>.
- [23] Marie-Fraïse Ponge, Olivier Poncelet, and Daniel Torrent. Dynamic homogenization theory for nonlocal acoustic metamaterials. *Extrem. Mech. Lett.*, 12:71–76, 2017. ISSN 2352-4316. doi: <https://doi.org/10.1016/j.eml.2016.10.006>. URL <http://www.sciencedirect.com/science/article/pii/S2352431616300979>.
- [24] Daniel Torrent, Yan Pennec, and Bahram Djafari-Rouhani. Resonant and nonlocal properties of phononic metasolids. *Phys. Rev. B*, 92(17):174110, 2015. doi: 10.1103/PhysRevB.92.174110. URL <https://link.aps.org/doi/10.1103/PhysRevB.92.174110>.
- [25] Yangyang Chen, Xiaopeng Li, Gengkai Hu, Michael R. Haberman, and Guoliang Huang. An active mechanical Willis meta-layer with asymmetric polarizabilities. *Nature Communications*, 11(1):3681, 2020. doi: 10.1038/s41467-020-17529-2. URL <https://doi.org/10.1038/s41467-020-17529-2>.
- [26] Joshua Lau, Suet To Tang, Min Yang, and Zhiyu Yang. Coupled Decorated Membrane Resonators with Large Willis Coupling. *Phys. Rev. Applied*, 12:014032, Jul 2019. doi: 10.1103/PhysRevApplied.12.014032. URL <https://link.aps.org/doi/10.1103/PhysRevApplied.12.014032>.
- [27] Anton Melnikov, Yan Kei Chiang, Li Quan, Sebastian Oberst, Andrea Alù, Steffen Marburg, and David Powell. Acoustic meta-atom with experimentally verified maximum Willis cou-

- pling. *Nature Communications*, 10(1):3148, 2019. doi: 10.1038/s41467-019-10915-5. URL <https://doi.org/10.1038/s41467-019-10915-5>.
- [28] Bogdan-Ioan Popa, Yuxin Zhai, and Hyung-Suk Kwon. Broadband sound barriers with bianisotropic metasurfaces. *Nature Communications*, 9(1):5299, 2018. doi: 10.1038/s41467-018-07809-3. URL <https://doi.org/10.1038/s41467-018-07809-3>.
- [29] Michael B. Muhlestein, Caleb F. Sieck, Preston S. Wilson, and Michael R. Haberman. Experimental evidence of Willis coupling in a one-dimensional effective material element. *Nature Communications*, 8:15625 EP –, 06 2017. URL <https://doi.org/10.1038/ncomms15625>.
- [30] Yongquan Liu, Zixian Liang, Jian Zhu, Lingbo Xia, Olivier Mondain-Monval, Thomas Brunet, Andrea Alù, and Jensen Li. Willis metamaterial on a structured beam. *Phys. Rev. X*, 9:011040, Feb 2019. doi: 10.1103/PhysRevX.9.011040. URL <https://link.aps.org/doi/10.1103/PhysRevX.9.011040>.
- [31] Aurélien Merkel, Vicent Romero-García, Jean-Philippe Groby, Jensen Li, and Johan Christensen. Unidirectional zero sonic reflection in passive \mathcal{PT} -symmetric Willis media. *Phys. Rev. B*, 98:201102, Nov 2018. doi: 10.1103/PhysRevB.98.201102. URL <https://link.aps.org/doi/10.1103/PhysRevB.98.201102>.
- [32] G W Milton, M Briane, and J R Willis. On cloaking for elasticity and physical equations with a transformation invariant form. *New J. Phys.*, 8(10):248, 2006. URL <http://stacks.iop.org/1367-2630/8/i=10/a=248>.
- [33] Graeme W Milton. New metamaterials with macroscopic behavior outside that of continuum elastodynamics. *New Journal of Physics*, 9(10):359–359, oct 2007. doi: 10.1088/1367-2630/9/10/359. URL <https://doi.org/10.1088%2F1367-2630%2F9%2F10%2F359>.
- [34] René Pernas-Salomón and Gal Shmuel. Symmetry breaking creates electro-momentum coupling in piezoelectric metamaterials. *Journal of the Mechanics and Physics of Solids*, 134:103770, 2020. ISSN 0022-5096. doi: <https://doi.org/10.1016/j.jmps.2019.103770>. URL <http://www.sciencedirect.com/science/article/pii/S0022509619306386>.
- [35] René Pernas-Salomón and Gal Shmuel. Fundamental principles for generalized willis metamaterials. *Physical Review Applied*, 14(6):064005, 2020.
- [36] René Pernas-Salomón, Michael R. Haberman, Andrew N. Norris, and Gal Shmuel. The electromomentum effect in piezoelectric willis scatterers. *Wave Motion*, page 102797,

2021. doi: <https://doi.org/10.1016/j.wavemoti.2021.102797>. URL <https://www.sciencedirect.com/science/article/pii/S0165212521000950>.
- [37] Alan Muhafra, Majd Kosta, Daniel Torrent, René Pernas-Salomón, and Gal Shmuel. Homogenization of piezoelectric planar willis materials undergoing antiplane shear. *Wave Motion*, 108:102833, 2022. ISSN 0165-2125. doi: <https://doi.org/10.1016/j.wavemoti.2021.102833>. URL <https://www.sciencedirect.com/science/article/pii/S0165212521001311>.
- [38] Zhizhou Zhang, Jeong-Ho Lee, and Grace X Gu. Rational design of piezoelectric metamaterials with tailored electro-momentum coupling. *arXiv preprint arXiv:2202.04275*, 2022.
- [39] Martin Philip Bendsøe and Ole Sigmund. *Topology Optimization: Theory, Methods and Applications*. Springer, February 2004. ISBN 9783540429920.
- [40] Martin P Bendsøe, JM Guedes, Robert B Haber, P Pedersen, and JE Taylor. An analytical model to predict optimal material properties in the context of optimal structural design. *Journal of Applied Mechanics*, 1994.
- [41] Jochem Zowe, Michal Kočvara, and Martin P Bendsøe. Free material optimization via mathematical programming. *Mathematical programming*, 79(1):445–466, 1997.
- [42] Michal Kočvara, Michael Stingl, and Jochem Zowe. Free material optimization: recent progress. *Optimization*, 57(1):79–100, 2008.
- [43] Ole Sigmund. Materials with prescribed constitutive parameters: an inverse homogenization problem. *International Journal of Solids and Structures*, 31(17):2313–2329, 1994.
- [44] Jan Stegmann and Erik Lund. Discrete material optimization of general composite shell structures. *International Journal for Numerical Methods in Engineering*, 62(14):2009–2027, 2005.
- [45] Bin Niu, Niels Olhoff, Erik Lund, and Gengdong Cheng. Discrete material optimization of vibrating laminated composite plates for minimum sound radiation. *International Journal of Solids and Structures*, 47(16):2097–2114, 2010.
- [46] J R Willis. Effective constitutive relations for waves in composites and metamaterials. *Proc. R. Soc. London A Math. Phys. Eng. Sci.*, 467(2131):1865–1879, 2011. ISSN 1364-5021. doi: 10.1098/rspa.2010.0620. URL <http://rspa.royalsocietypublishing.org/content/467/2131/1865>.
- [47] Andrea Alù. First-principles homogenization theory for periodic metamaterials. *Physical Review B*, 84(7):075153, 2011.

- [48] C. Fietz and G. Shvets. Metamaterial homogenization: extraction of effective constitutive parameters. *Proc. SPIE 7392, Metamaterials: Fundamentals and Applications II*, page 73920L, 2009. doi: 10.1117/12.827031.
- [49] Chris Fietz and Gennady Shvets. Current-driven metamaterial homogenization. *Physica B: Condensed Matter*, 405(14):2930 – 2934, 2010. ISSN 0921-4526. doi: <https://doi.org/10.1016/j.physb.2010.01.006>. URL <http://www.sciencedirect.com/science/article/pii/S0921452610000086>. Proceedings of the Eighth International Conference on Electrical Transport and Optical Properties of Inhomogeneous Media.
- [50] Andrea Alù. First-principles homogenization theory for periodic metamaterials. *Phys. Rev. B*, 84:075153, Aug 2011. doi: 10.1103/PhysRevB.84.075153. URL <https://link.aps.org/doi/10.1103/PhysRevB.84.075153>.
- [51] John R. Willis. The construction of effective relations for waves in a composite. *Comptes Rendus Mécanique*, 340(4):181 – 192, 2012. ISSN 1631-0721. doi: <https://doi.org/10.1016/j.crme.2012.02.001>. URL <http://www.sciencedirect.com/science/article/pii/S1631072112000381>. Recent Advances in Micromechanics of Materials.
- [52] René Pernas-Salomón and Gal Shmuel. Fundamental Principles for Generalized Willis Metamaterials. *Phys. Rev. Applied*, 14:064005, Dec 2020. doi: 10.1103/PhysRevApplied.14.064005. URL <https://link.aps.org/doi/10.1103/PhysRevApplied.14.064005>.
- [53] Graeme W. Milton. A unifying perspective on linear continuum equations prevalent in physics. part iv: Canonical forms for equations involving higher order gradients. *arXiv: Mathematical Physics*, 2020.
- [54] Andrea Alù. Restoring the physical meaning of metamaterial constitutive parameters. *Phys. Rev. B*, 83:081102, Feb 2011. doi: 10.1103/PhysRevB.83.081102. URL <https://link.aps.org/doi/10.1103/PhysRevB.83.081102>.
- [55] René Pernas-Salomón, Michael R Haberman, Andrew N Norris, and Gal Shmuel. The electromomentum effect in piezoelectric willis scatterers. *Wave Motion*, 106:102797, 2021.
- [56] M S Kushwaha, P Halevi, L Dobrzynski, and B Djafari-Rouhani. Acoustic band structure of periodic elastic composites. *Phys. Rev. Lett.*, 71(13):2022–2025, 1993.
- [57] M M Sigalas and E N Economou. Attenuation of multiple-scattered sound. *Europhys. Lett.*, 36(4):241–246, 1996. doi: 10.1209/epl/i1996-00216-4.

- [58] René Pernas-Salomón and Gal Shmuel. Dynamic homogenization of composite and locally resonant flexural systems. *J. Mech. Phys. Solids*, 119:43–59, 2018. ISSN 0022-5096. doi: <https://doi.org/10.1016/j.jmps.2018.06.011>. URL <http://www.sciencedirect.com/science/article/pii/S0022509618302503>.
- [59] Krister Svanberg. The method of moving asymptotes - a new method for structural optimization. *Int. J. Numer. Methods Eng.*, 24:359–373, 1987.
- [60] Lingling Wu, Yong Wang, Kuochih Chuang, Fugen Wu, Qianxuan Wang, Weiqi Lin, and Hanqing Jiang. A brief review of dynamic mechanical metamaterials for mechanical energy manipulation. *Materials Today*, 44:168–193, 2021. ISSN 1369-7021. doi: <https://doi.org/10.1016/j.mattod.2020.10.006>. URL <https://www.sciencedirect.com/science/article/pii/S1369702120303618>.
- [61] Srajan Dalela, P. S. Balaji, and D. P. Jena. A review on application of mechanical metamaterials for vibration control. *Mechanics of Advanced Materials and Structures*, 0(0):1–26, 2021. doi: 10.1080/15376494.2021.1892244. URL <https://doi.org/10.1080/15376494.2021.1892244>.